Dynamic Hydrogen Bubble Template Electrodeposited Bi on Graphite Felt and the Effect of its Post-processing in Vanadium Redox Flow Batteries

Ming Cheng, Tintula Kottakkat *, Christina Roth

Electrochemical Process Engineering, University of Bayreuth, Universitätsstraße 30, 95447 Bayreuth, Germany

* Corresponding author email: tintulakk@gmail.com

Keywords

Vanadium redox flow battery, Bismuth catalyst, Dynamic hydrogen bubble template electrodeposition, Negative graphite felt electrode, $V^{2+/3+}$ redox couple

Abstract

In this work, the very effective synthesis method of dynamic hydrogen bubble template (DHBT) electrodeposition has been first time employed in decorating graphite felt (GF) with high surface area bismuth nanoparticles as the negative electrode in vanadium redox flow batteries (VRFBs). The electrodes synthesized by the DHBT method were compared with other reported systems, such as Bi_2O_3 particles impregnated on GFs and adding Bi^{3+} directly into the vanadium electrolyte. In this comparison, the DHBT-synthesized samples showed significantly improved kinetics of the V^{3+}/V^{2+} redox reactions. Besides, it can be demonstrated that the performance is significantly affected by the post-processing and drying conditions of the synthesized electrode owing to alterations in morphologies, distributions of Bi, impurities, etc. Precise kinetic analysis was performed using cyclic voltammetry (CV) and electrochemical impedance spectroscopy (EIS) normalization in a 3-electrode setup. Surface morphology, catalyst composition and stability were characterized by scanning electron microscopy (SEM), energy dispersive X-ray spectroscopy (EDX), X-ray diffraction (XRD) and inductively coupled plasma-optical emission spectroscopy (ICP-OES), respectively. Full-cell polarization tests demonstrated that the air dried DHBT Bi modified graphite felt electrode as negative electrode could achieve a power density of 416.6 mW·cm^{-2} at a current density of 480 mA·cm^{-2}. Additionally, the observed electrolyte utilization is reported as high as 37.5 Ah·L^{-1}, while the energy efficiency stabilized at around 78% after 100 cycles at a current density of 25 mA·cm^{-2}.

1. Introduction

Global climate change is one of the most considerable challenges of the 21st century due to a large amount of greenhouse gas emissions released into the atmosphere as a result of human activities [1]. In order to realize a low-carbon economy and cut down on greenhouse gas emissions, conventional fossil-based energy needs to be replaced by renewable energy sources, such as solar energy, wind energy, etc. in the immediate future [2][3]. In the meanwhile, large-scale energy storage systems will be required to be well developed for solving the issues of only intermittently available renewable energy supply and stabilizing the power grid. Redox flow batteries (RFBs) are considered as suitable candidates for reliable and large-scale energy storage due to their scalability, high storage capacity, long cycle life, fast response time, high efficiency, decoupled energy and power, etc. Among all the RFB types, the technology of vanadium redox flow batteries

(VRFBs) appears to be the most established to-date and has already been commercialized for many years. The largest advantage of VRFBs is that they effectively avoid cross-contamination by employing the same element, i.e., vanadium, in both anolyte and catholyte [4][5][6]. However, their mass-market commercialization is still hindered by their high capital cost and low energy density [7][8].

To improve their performance, the utilized electrodes, as important components of VRFBs, play a significant role as they not only affect the mass transport but also provide active sites for the vanadium redox reactions. At present, the most widely used electrode materials in VRFBs with flow-through channels are three-dimensionally structured graphite felts (GFs) owing to their high surface area, chemical stability, and good electrical conductivity [8]. However, their poor electrochemical activity and hydrophobicity limit the performance, when pristine GFs are being used. Furthermore, the V^{3+}/V^{2+} redox couple at the negative side has been widely reported to be the more kinetically hindered one in VRFBs and thus contributes more to the cell overpotential during discharge than the positive side reactions [9][10][11]. For these reasons, different pretreatment methods for GFs, such as thermal treatment [12], acid treatment [13], KOH treatment [14], or introducing metal-based electrocatalysts, such as bismuth [15][16][17][18][19][20][21], neodymium [22], iridium [23], titanium [24][25][26] were investigated and found to improve the kinetics at the negative side. Particularly, bismuth and bismuth compounds have been widely reported to be promising catalysts for the V^{3+}/V^{2+} redox reaction. For instance, in 2013 Li *et al.* reported for the first time that adding 0.01 M BiCl$_3$ into the vanadium electrolyte can not only increase the electrolyte utilization by 30 % but also improve the energy efficiency (EE) [15]. However, this method of adding certain concentrations of bismuth to a large volume of electrolyte in order to deposit at the electrode and form active sites for the catalysis of the V^{3+}/V^{2+} redox reaction results in a very low bismuth utilization as well as it adds additional cost. Schneider *et al.* impregnated Bi$_2$O$_3$ onto the GF and studied the degradation phenomena by EIS [17]. The experiments excluded additional effects caused by the other applied pretreatment methods, such as heat treatment, immersion in acetic acid and ammonium hydroxide, and confirmed that the presence of bismuth can indeed enhance the kinetics of the V^{3+}/V^{2+} reaction. The authors also proposed that the presence of bismuth can accelerate the degradation of the graphite fibers by testing the GF in a 3-electrode setup after 50 cycles in a full cell. Unfortunately, the paper did not mention the exact location in which the electrode degradation was observed. The method of decorating GF by Bi$_2$O$_3$ impregnation normally leads to an only uneven distribution of Bi$_2$O$_3$, which correlates with an uneven current distribution in the full-cell test. This would eventually cause some parts of the electrode to deteriorate more severely than the others and would therefore be a more indirect degradation effect of the Bi itself. Another important issue are the post-processing and drying conditions when fabricating battery electrodes, which can largely affect the morphology, distribution, impurities, etc. of the electrocatalyst and consequently the full-cell performance. Kumberg *et al.* have studied the effect of various drying parameters at anodes in lithium-ion batteries [27]. The drying process after wet film coating of rather thick electrodes was described by film shrinkage, capillary transport of the liquid and evaporation of the liquid clusters within the porous structure. It was also pointed out in this study that the drying process of thick electrodes is still challenging because of drying rate, adhesion and crack formation issues.

According to the literature of the past decades, effective synthesis methods for the homogeneous deposition of Bi on carbonaceous electrode materials were rarely studied and reported. More essentially, seldom effort has been undertaken to systematically investigate the influence of post-processing and drying conditions on the synthesized electrode in vanadium redox flow batteries. In this work, dynamic hydrogen bubble template (DHBT) electrodeposition was employed as a very effective strategy to electrodeposit Bi on GFs in a controlled fashion. Previously, DHBT was

developed by Shin *et al*. for Cu or Cu-based foams [28], then extended to Ag-based systems [29] and recently Bi-based foams were also developed with this approach [30]. The synthesized samples by DHBT have been investigated and applied in the area of electrochemical CO_2 reduction reaction (CO_2RR) [30], biosensors [31], supercapacitors [32], etc. This rather facile approach utilizes the generation of hydrogen bubbles at high negative overpotentials as a dynamic template to deposit high surface area metal foams. Herein, we report for the first time the DHBT synthesis of Bi nanoparticulate foam structures as electrocatalysts on pristine electrode materials for their application in VRFBs. The changes in their electrocatalytic activity before and after Bi modification were investigated by cyclic voltammetry (CV), electrochemical impedance spectroscopy (EIS), full-cell polarization and cycling tests. The performance of the electrodes by DHBT was compared with other reported systems, such as Bi_2O_3 impregnation on GFs [17] and Bi^{3+} directly present in the vanadium electrolyte as a homogenous catalyst [15][18]. The kinetic parameters were determined qualitatively by using the EIS normalizing method proposed by Friedl and his coworkers [33][34]. The surface morphology, microstructure and Bi stability were characterized in detail by scanning electron microscopy (SEM), energy dispersive X-ray spectroscopy (EDX), X-ray diffraction (XRD) and inductively coupled plasma-optical emission spectroscopy (ICP-OES). Besides, this study focused on the effect of post-processing treatments after Bi electrodeposition and how they will influence performance-deciding factors, such as the morphology, electrochemically active surface area (ECSA), distribution of Bi and impurities present, etc. In the full-cell tests, a flow-through type VRFB with the optimized DHBT-Bi deposit on GF showed high energy efficiency (EE) and electrolyte utilization.

2. Experimental section

2.1 Materials

To study the morphologies and electrochemical properties of the Bi-metal foam, both 2-D structured glassy carbon (GC) and 3-D structured pristine graphite felt (GF) were used as electrodeposition substrates. The following sizes of substrate materials have been used for Bi electrodeposition: (i) 1 cm x 1 cm glassy carbon (GC, Hochtemperatur-Werkstoffe GmbH); (ii) pristine graphite felt (GF, GFD 4.6, SGL carbon group, Germany) with the diameter of 8 mm. The standard electrodeposition bath for Bi foam synthesis was composed of 30 mM Bi^{3+} by dissolving Bi_2O_3 (Alfa Aesar, USA) into 2 M HNO_3 (Sigma-Aldrich Chemie GmbH, Germany) serving as the supporting electrolyte.

The half-cell used was a glass compartment comprising 3 electrodes and one inert gas purging tube. The working electrodes (WE) were either Bi deposited GCs or GFs. Ag/ AgCl (RE, XYLEM Analytics Germany GmbH, Germany) refers to 198 mV vs. standard hydrogen electrode (SHE) was used as reference electrode (RE). A piece of GF with the size of 1 cm x 2 cm was employed as the counter electrode (CE). The V^{3+}/V^{2+} electrolyte was prepared from commercial electrolyte 1.6 M V^{3+}/VO^{2+} (GfE GmbH, Germany). For electrochemical characterization, 0.16 M V^{3+}/V^{2+} in 2 M H_2SO_4 (Carl Roth, Germany) was used for half-cell measurements and 1.6 M V^{3+}/V^{2+} was used for full-cell measurements.

2.2 Electrochemical deposition

The Bi electrodeposition was carried out in a glass beaker with 80 ml 30 mM Bi^{3+}/ 2 M HNO_3 solution by applying a current density of j= -200 mA·cm^{-2} for 300 s (refer to the geometric surface area of the substrates). The WE and CE were face to face at a distance of 1 cm. Due to the hydrophobicity of the pristine GFs, they were centrifuged in corresponding solutions at 2500 rpm

for 5 mins before electrodeposition in order to make sure that the tiny pores are filled with the solution. The GFs after Bi deposition were rinsed in water for short time for washing out the residues from the deposition bath and then dried overnight at room temperature to remove the absorbed water from the pores of the GF so that the catalysts particles form a stable final structure on the graphite fibers. In the latter part of the paper, the influence of the post-processing, such as air or vacuum drying, exposure duration to water during the rinsing step, etc. are discussed.

2.3 Electrochemical characterization

Measurements in a 3-electrode setup including the CV, EIS and ECSA were performed with a Gamry Reference 600 potentiostat. In all half-cell electrochemical measurements, the electrolyte was initially purged with Ar for 15 min to remove the residual air in the electrolyte and maintain an Ar atmosphere above the electrolyte. CV measurements were performed at a scan rate of 4 mV·s^{-1} within the scan limits which can completely present both reduction and oxidation peaks for specific samples. Three cycles were measured and the third cycle was taken for analysis. Potentiostatic EIS measurements were conducted within a frequency range of 10^5-10^{-1} Hz employing an AC amplitude of 10 mV. The DC potential was set to be -0.49 V vs. Ag/AgCl. ECSA were obtained by measuring CVs in the non-faradaic region from -0.35 V to -0.45 V at different scan rates of 50, 100, 150, 200, 250, 300, 350, 400 mV·s^{-1}.

The full-cell experiments were performed in a redox flow battery system (857 Redox Flow Test System; Scribner Associates, USA). 60 ml electrolyte was circulated into each of the two tanks with a flow rate of 70 ml·min^{-1}. A single flow-through cell with an electrode area of 4 cm^2 was assembled for full-cell tests. To avoid the positive side becoming the limiting side, thermally activated instead of pristine GFs were used as the positive side electrode. At the negative side, either pristine GF or Bi decorated pristine GF by DHBT was used to study the catalytic effect of Bi. An anion exchange membrane (FAP 450; Fumatech, Germany) was employed to avoid cation cross-over and contamination. Ar was constantly purged to keep the system under inert conditions. The polarization curve was tested with 100 % SOC electrolyte. Polarization and power curves were measured with the current scan step of 20 mA·cm^{-2} and at each point lasted for 5 s. During the cycling tests, the cutoff voltages were set to values from 1 V to 1.65 V.

2.4 Structural and compositional characterization

(i) The morphologies and distribution of the Bi modified GCs and GFs by DHBT were characterized by using the Zeiss Ultra plus with a high-resolution field emission gun scanning electron microscope (SEM, Zeiss, Germany) at the Bavarian Polymer Institute (BPI) in the University of Bayreuth. An Inlens SE-detector (secondary electron), Inlens EsB-detector (energy selective backscattered electrons) and Ultra Dry EDX detector (energy dispersive X-ray spectroscopy) were used to perform the SE, BSE and EDX results. The acceleration voltage was set to be 3 kV.
(ii) Empyrean system (PANalytical B.V.) with a reflection transmission spinner was used for XRD analysis. The radiation source is Cu k$_\alpha$ (λ_k$_{\alpha1}$ = 1.5406 Å ; λ_k$_{\alpha2}$= 1.54443 Å), and the generator current and voltage were set to be 40 mA and 40 kV, respectively. Diffractograms were recorded with a fixed anti-scattering slit of 1° and a fixed divergence slit of 0.5°, with 2θ values ranging from 10° to 90°. For the XRD analysis of the Bi/GFs under different drying conditions, the bulk GF samples were firstly squeezed to lose fibers in order to be flush with the Si single crystal sample holder and be well suited to the XRD equipment for the measurement. The obtained XRD patterns were analyzed and compared to Joint Committee on Powder Diffraction standards (JCPDS) data for polycrystalline Bi (ICDD-PDF-2021-01-085-5855), Bi$_2$O$_3$ (ICDD-PDF-2021-04-005-4873) and GF (ICDD-PDF-2021-00-058-1638).

(iii) ICP-OES (Optima 7300 DV, PerkinElmer Inc., US) measurements were carried out to probe the amount of Bi after electrodeposition and the dissolution after cycling in half-cell and full-cell tests. Prior to the ICP-OES measurement, aqua regia was prepared to digest the Bi on the GFs. Then the solution was diluted to a level that would match the range of the calibration curve. After the ICP-OES analysis, the actual amount of Bi on the GF electrode can be recalculated.

3. Results and discussion

3.1 Synthesis and optimization of porous Bi foams on glassy carbon (GC) and graphite felt (GF)

The working principle of the dynamic hydrogen bubble template (DHBT) is illustrated in Figure 1. In this study, $Bi(NO_3)_3$ solution was used as the deposition bath due to the good dissolution of Bi_2O_3 in HNO_3. Bi^{3+} in the electrodeposition bath is reduced to Bi, while H^+ is reduced to H_2 bubbles in the aqueous $Bi(NO_3)_3$ solution under sufficiently cathodic overpotential. Equations (1) and (2) show the reduction reactions and their standard potentials, respectively. The H_2 bubbles generated from the surface of the substrate tend to grow into larger bubbles while rising towards the electrolyte surface, due to less pressure. During this process, the bubbles work as a dynamic template for the Bi electrodeposition. Bi particles will deposit and grow around the bubbles, thereby generating a hierarchically porous Bi structure with maximized specific surface area [35]. Bi was electrodeposited on both 2-D structured GC and 3-D structured GF to study the properties of the final Bi foam. Besides, the effect of DHBT itself on the GF (i.e. polarizing the GF to negative potentials) has been studied by using the supporting electrolyte 2 M HNO_3 without any Bi, as shown in Figure S1. The GF was polarized to the same negative potentials for the same amount of time as done in the normal Bi foam synthesis procedure. It has been verified that the polarization of GF to negative potentials could only induce corrosion and thereby roughen the felt surface but without any significant catalytic effect.
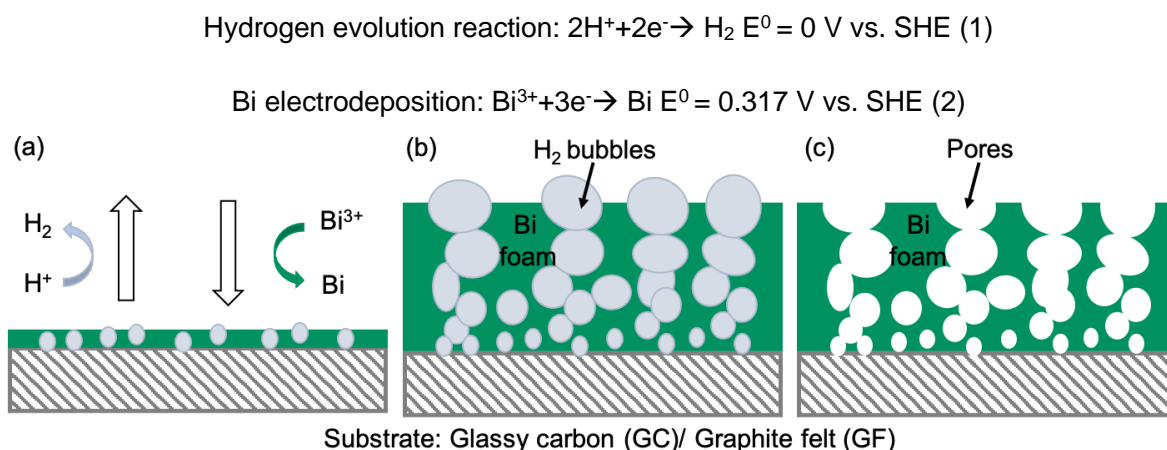
$$\text{Hydrogen evolution reaction: } 2H^+ + 2e^- \rightarrow H_2 \quad E^0 = 0 \text{ V vs. SHE (1)}$$

$$\text{Bi electrodeposition: } Bi^{3+} + 3e^- \rightarrow Bi \quad E^0 = 0.317 \text{ V vs. SHE (2)}$$

Figure 1. Working principle of DHBT method: (a) at sufficient cathodic overpotential, Bi^{3+} in 30 mM $Bi(NO_3)_3$ solution is reduced to Bi, while H^+ is reduced to H_2 bubbles; (b) H_2 bubbles act as dynamic bubble template for Bi foam growth on the substrate; (c) hierarchically porous Bi structures are being formed.

There are two essential parameters during the synthesis, i) the supplied cathodic current and ii) the electrodeposition time, which largely influence the morphology and thus the performance of the Bi foam. When the applied absolute current is very small, only few and tiny H_2 bubbles can be generated resulting in an undesirably compact foam. On the contrary, if the supplied absolute current is very high, many and large H_2 bubbles will be produced causing fragile structures to form

and consequently resulting in the instability of the electrodeposited Bi foam. Electrodeposition time has also a large impact since it determines the amount of Bi deposited on the substrate as well as the thickness of the foam. In this work, the most efficient deposition time has been determined based on a suitable cathodic current density with respect to the resulting V^{3+}/V^{2+} peak current from the CV and ECSA measurements. The ECSA is obtained by correlating the double-layer capacitance (DLC) to the active surface area. DLC is determined by measuring CVs in the non-faradaic region at different scan rates in order to derive the slope of the absolute average current vs. scan rate curve. The relative ECSA can be determined from the following equation:

$$ECSA = C_{dl}/\,C_{ref} \cdot A_{ref,geo} \quad (3)$$

A planar tip electrode composed of pure Bi metal with a diameter of 5 mm is used as a reference here and the experimental DLC for this reference is $C_{ref}= 39\ \mu F$.

Figure 2 (a-c) depicts exemplary SEM images of electrodeposited Bi foam on GC at different magnifications. From these, highly interconnected porous walls and numerous Bi nanoparticles on GC can be observed. The sizes of the particles range from 200 nm to 350 nm, indicating a greatly enhanced surface area. However, in comparison with SEM images of the Bi foam in the literature, such as the Bi foam deposited on carbon fiber cloth reported by Dutta et al. [30], the size of the surface pores here is only about one-tenth of that reported in the respective literature, which is mainly due to the chosen deposition parameters, namely, the much smaller applied current density and the longer deposition time in our synthesis. Since 3-D structured porous pristine GFs are the target substrate material and would be finally tested in the full-cell setup, large volumetric and areal densities of Bi nanoparticles are required so that reproducibly and robustly adhere to the graphite fibers. Therefore, a relatively smaller current density and longer deposition times appear to be more suitable. Figure 2 (d-f) shows the Bi distribution on the graphite fibers with the electrodeposition time of 75 s, 150 s, 300 s at a current density of 200 mA·cm^{-2} by DHBT. It shows that thin Bi layers, or at least extended Bi patches, are formed and well distributed on the graphite fibers. Within 300 s deposition time, the longer the electrodeposition time, the better the distribution of Bi on the GF fibers. As observed in Figure 2 (f), there are more Bi nanoparticles on the fibers, but first Bi agglomerations are observed when the deposition time approaches 300 s and above. Therefore, the deposition time should be well controlled to avoid undesirable Bi agglomerates. A higher magnification SEM image of nano-structural Bi on GFs is provided in Figure S3 (a) which shows the effectiveness of the DHBT electrodeposition on 3D substrates.
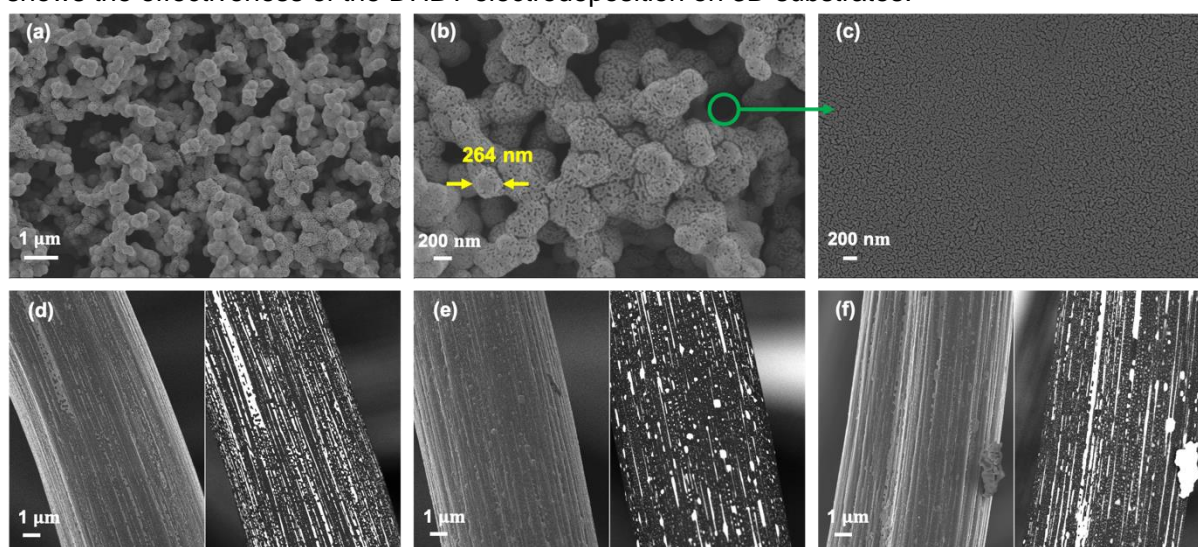

Figure 2. (a-c) Different magnification SEM images of electrodeposited Bi by DHBT method on GC. BSE images of electrodeposited DHBT-Bi on GF in 30 mM Bi^{3+}/2 M HNO$_3$ at an applied current density

of 200 mA·cm^{-2} with an electrodeposition time of (d) 75 s; (e) 150 s; (f) 300 s. All the samples were dried under air at room temperature overnight before measuring in the SEM.

Figure 3 (a) shows the ECSA of the Bi foams on GC with different electrodeposition times, using a planar Bi-metal tip electrode as a reference. The dependence of double layer charging current on scan rates and the CV curves of GCs with different Bi electrodeposition time are summarized in Figure S2. Figure 3 (b) shows the double-layer capacitance current as a function of the scan rate of Bi/GFs at various electrodeposition times. The ECSA of Bi-modified GF cannot be easily determined, because neither GC nor Bi metal are suitable references. Nevertheless, the slopes reflect the relative change of ECSA with different electrodeposition times. Bi electrodeposition on both GC and GF exhibits a pronounced increase in ECSA compared to that of a pristine GC or GF. Besides, it was found that the ECSA is proportional to the electrodeposition time. However, the difference in DLC among the Bi/GFs with different deposition times is not so easy to observe. A clear increasing trend only started to become visible when the deposition time was more than 300 s. Figure S3 illustrates the CV curves of Bi/GFs with different electrodeposition time. Figure 3 (c) and (d) summarize the normalized V^{3+}/V^{2+} oxidation and reduction reaction peak currents with respect to the ECSA of Bi/GCs or to the slope of double layer capacitance current to the scan rate of Bi/GFs as a function of electrodeposition time, respectively. The oxidation peak current density is the highest when the electrodeposition time is from 300 s to 400 s on GFs, while the highest reduction current density is observed when the deposition time is 300 s. Therefore, 300 s electrodeposition time was chosen for all further sample syntheses. Besides, it was found that the current densities of GFs are much higher than those of GCs, which should be beneficial from the original 3-D porous structure of GFs. All the DLC, ECSA, peak currents, and ECSA normalized current densities of Bi/GCs and Bi/GFs with different electrodeposition time are summarized in Table S1 and Table S2.
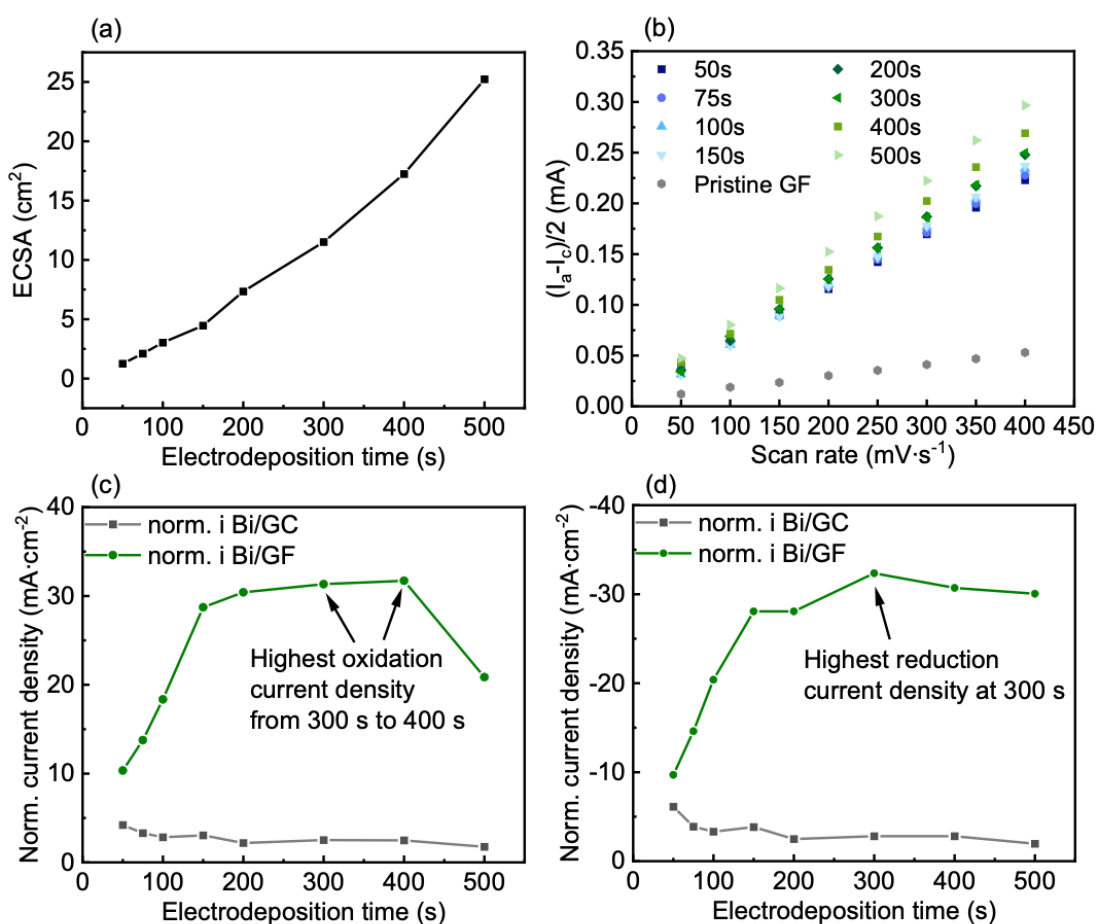
Figure 3. (a) ECSA of Bi/GCs with different electrodeposition times. (b) Double layer capacitance current of Bi/GFs from CV measurements in the non-faradaic region at -0.4 V vs. Ag/AgCl as a function of scan rates. (c) Normalized V^{3+}/V^{2+} oxidation reaction peak currents of Bi/GC and Bi/GF with different electrodeposition times. (d) Normalized V^{3+}/V^{2+} reduction reaction peak currents of Bi/GCs and Bi/GFs with different electrodeposition times. All the Bi/GFs after synthesis were dried under air at room temperature overnight before testing in 0.16 M V^{3+}/ V^{2+}/ 2 M H_2SO_4 electrolyte.

3.2 Comparison of DHBT method with Bi_2O_3 impregnation and Bi^{3+} in the electrolyte

The DHBT-Bi modified GF is compared with other reported systems including Bi_2O_3 impregnation on GFs [17] and Bi^{3+} directly added to the vanadium electrolyte as homogeneous catalysts [15]. The amount of Bi was controlled to be the same in all three systems. In view of the high reproducibility and comparability of the results, the Bi_2O_3 nanoparticles (US Research Nanomaterials) used here exhibit a uniform nanoparticle size of 80 nm, also comparable to the respective literature reports. CV measurements and EIS normalization as first proposed by Friedl and co-workers were combined to obtain precise kinetic parameters [33][34] in order to compare the different types of Bi involving systems. The EIS normalization method correlates the charge transfer resistance R_{ct} and double layer capacitance C_{dl} from impedance measurements. A simple Randle's model which is composed of an ohmic resistance R_{ohm} and in series to a parallel combination of charge transfer resistance R_{ct} and double layer capacitance C_{dl}: R_{ohm}-(R_{ct} | C_{dl}) was built. According to the mathematical equations, the slope from the relation of C_{dl} and R_{ct}^{-1} can indicate the exchange current density, as follows.

$$C_{dl} = \epsilon_r \epsilon_0 \frac{A_{wet}}{t_{dl}} \ (4)$$

$$R_{ct} = \frac{RT}{nF j_0 A_{wet}} \ (5)$$

$$R_{ct}^{-1} = \frac{nF t_{dl}}{RT \epsilon_r \epsilon_0} j_0 C_{dl} \ (6)$$

Where A_{wet} is the wetted surface area; R is the gas constant; T is the absolute temperature; n is the number of transferred electrons; F is Faraday's constant; ϵ_r is the relative dielectric permittivity; ϵ_0 is the permittivity of the free space; t_{dl} is the thickness of the double layer; j_0 is the exchange current density.

The CV curves of GFs with and without Bi are illustrated in Figure 4 (a). It is found that the system without Bi shows the poorest electrochemical activity towards the V^{3+}/V^{2+} redox reactions according to the large peak separation and low peak height. For the systems with Bi involved, either by decorating the Bi with DHBT or with Bi_2O_3 impregnation onto the GFs or adding Bi^{3+} directly into the electrolyte, the peak separations decrease significantly, suggesting a better wettability and enhanced kinetics due to the presence of Bi. More notably, electrodeposited DHBT-Bi on GFs improves the kinetics of V^{3+}/V^{2+} redox reactions the most effectively, as observed from the lowest peak separation and the highest peak height. The peak separation of the GFs with Bi_2O_3 impregnation is also quite small, most probably due to the originally uniform 80 nm particle sizes. However, the peak height is much lower for GFs with Bi_2O_3 impregnation than for the other two systems, which indicates that the V^{3+}/V^{2+} conversion is rather low. Another disadvantage of the Bi_2O_3 impregnation method is that the Bi_2O_3 particles are difficult to distribute uniformly on the surface and into the pores of the GFs directly after synthesis. As for the method of adding Bi^{3+} directly into the vanadium solution, the kinetics of V^{3+}/V^{2+} redox reactions are not improved significantly, which might correlate with Bi^{3+} diffusion and deposition processes and with the fact that Bi_2O_3 does not dissolve easily in 2 M H_2SO_4 based vanadium electrolyte. Therefore, the first

deposition occurs also rather inhomogeneous and the Bi is only dissolved and re-deposited more uniformly after the first cycle.
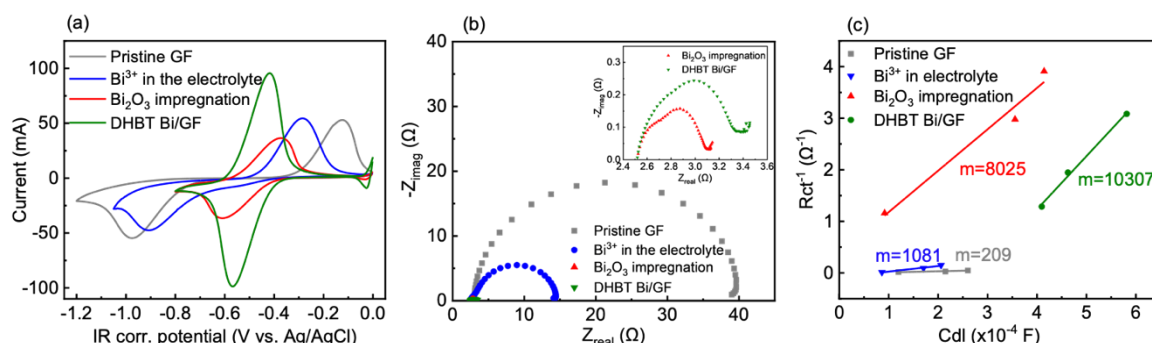

Figure 4. Comparison of systems without Bi (gray, pristine GF), with Bi on GF by DHBT (green, under air drying after synthesis), Bi_2O_3 impregnation on GF (red), and Bi^{3+} added directly into the electrolyte (blue). The amounts of Bi were controlled to be the same in all three systems. (a) CV curves of V^{3+}/V^{2+} redox reactions at 4 mV·s^{-1}. (b) Nyquist plots at the open circuit potential of -0.5 V vs. Ag/AgCl. (c) Inverse charge transfer resistance vs. double layer capacitance by EIS normalization.

Nyquist plots in Figure 4 (b) indicate the improved performance for all the systems with Bi involved, according to the reduced diameters of the semicircles in EIS representing a smaller charge transfer resistance R_{ct}. However, it is not possible to directly confirm that such an improvement is directly caused by altered kinetics, since the wettability of the electrodes does also play a role here. To properly consider this additional effect, EIS has been conducted on electrodes of 3 different sizes (φ: 6 mm, 8 mm, 10 mm) as suggested previously by Friedl et al. [33][34] for each type of Bi system. The diameter of the semicircles in the Nyquist plot should decrease with an increased sample size. EIS data were fitted with Randle's model R_{ohm}-(R_{ct} | C_{dl}) as mentioned above within the frequency range of 10^4-1 Hz. Linear relations between the R_{ct}^{-1} and C_{dl} were determined for all samples under investigation. As shown in equation (6) the slopes of the normalized EIS data reveal trends in the exchange current density j_0. The normalized EIS results are illustrated in Figure 4 (c). In contrast to the system without Bi, the other three systems with Bi have all improved to various degrees. Among them, the electrode synthesized by DHBT shows the highest slope. Bi_2O_3 impregnation comes second, while adding the Bi^{3+} directly into the electrolyte results in the least improvement. This result coincides with the conclusion derived from the peak separations in CV curves confirming the validity of our observations.

3.3 Stability test

The stability of electrodeposited Bi nanoparticles on GFs is essential for the viability of our suggested preparation strategy and for industrial implementation in VRFBs. A stable catalyst needs to withstand the highly corrosive electrolyte environment and should not be easily flushed away by the flowing electrolyte, either. Therefore, to get a first indication of catalyst stability, 200 cycles of CV at a scan rate of 4 mV·s^{-1} have been performed with a DHBT-Bi/GF in 0.16 M V^{3+}/ V^{2+}/ 2 M H_2SO_4 electrolyte with a 3-electrode setup. As shown in Figure 5, a slight decrease in the peak height can be observed for the 200th cycle which amounts to about 82 % peak current of the 1st cycle. Moreover, the close peak separation is maintained over time. The dissolution of Bi has been studied by means of ICP-OES, and it has been found that about 65% of Bi stays on the GF, while the rest is dissolved in the electrolyte. The specific amounts of Bi before and after the stability test are provided in the supplementary part.
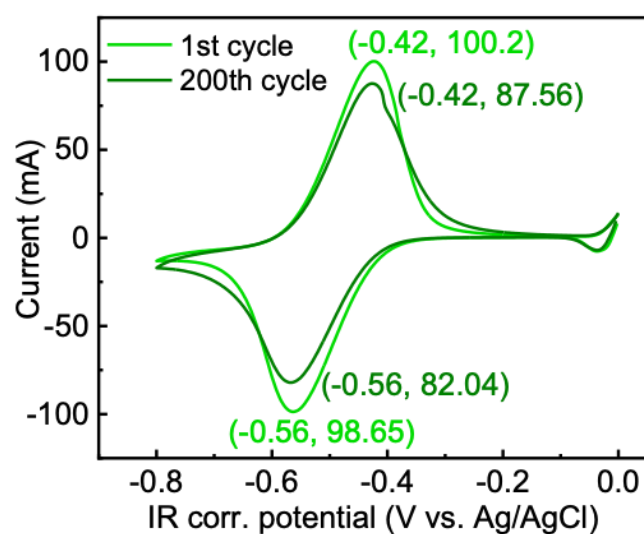
Figure 5. Stability test of DHBT-Bi/GF (under air drying after synthesis) by measuring 200 cycles of CV at a scan rate of 4 mV·s^{-1} with a 3-electrode setup in 0.16 M V^{3+}/ V^{2+}/ 2 M H$_2$SO$_4$ electrolyte.

3.4 DHBT-Bi/GFs under different post-processing and drying conditions

DHBT-Bi/GFs after synthesis need to be removed from the aqueous electrodeposition bath and dried before measuring in the V^{3+}/V^{2+} electrolyte. We found that different post-processing and drying conditions can cause different morphologies, ECSA, Bi distributions and degrees of oxidation, etc. which in turn can result in different electrochemical performances towards the V^{3+}/V^{2+} redox reactions. A possible mechanism of the drying processes is presented in Figure 6. The freshly synthesized GFs decorated with Bi are shown in Figure 6 (a). Ideally, Bi should homogeneously adhere to the graphite fibers and a layer of Bi foam is deposited on the surface of the GF. When the Bi/GF is removed from the electrodeposition bath, it is assumed that the Bi/GF would shrink and "deflate", because the bubbles would break due to the pressure difference between air and liquid. Then, some of the voids left by the bubbles will refill with solvent, as illustrated in Figure 6 (b). With the ongoing drying process, connected channel networks of solvent-filled capillaries will evolve. From these, the solvent gets transported within the microstructure and will evaporate when near to the surface of the foam. In contrast, some of the liquid clusters which are not connected to this capillary network will lose their liquid contents within the porous structure, forming slugs and diffusing through the dried particle pores (Figure 6 (c)) [27]. In the end, the dried Bi foam of reduced thickness or at least its fragments will adhere to the graphite fibers as shown in Figure 6 (d).
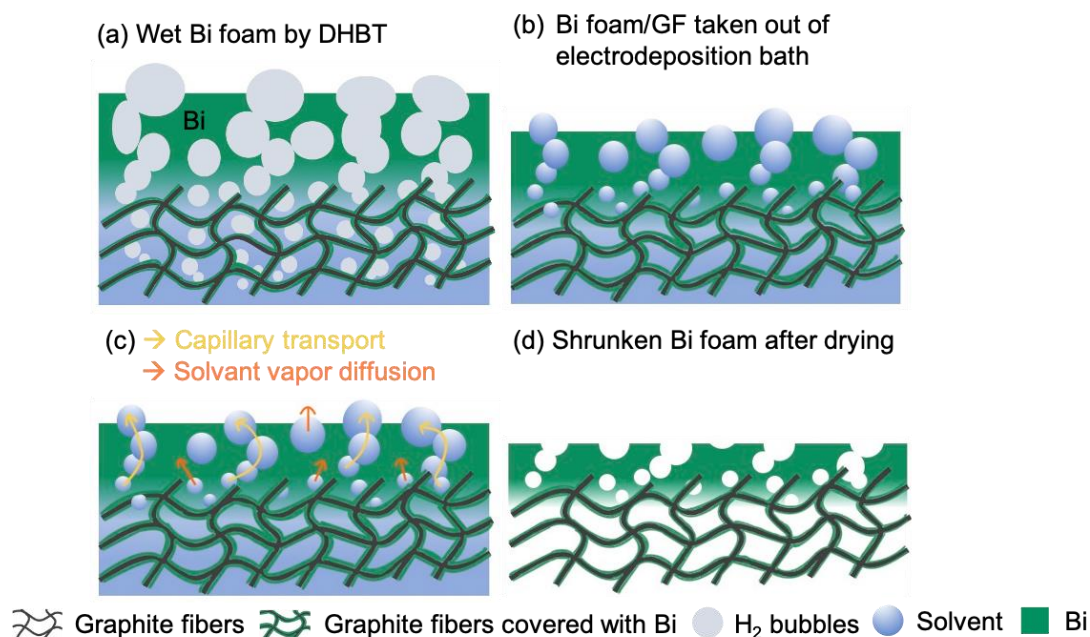
(a) Wet Bi foam by DHBT

(b) Bi foam/GF taken out of electrodeposition bath

(c) → Capillary transport
    → Solvant vapor diffusion

(d) Shrunken Bi foam after drying

Graphite fibers   Graphite fibers covered with Bi   H$_2$ bubbles   Solvent   Bi

Figure 6. The drying process of a DHBT-Bi foam on GF: (a) freshly synthesized Bi foam on GF in 30 mM Bi(NO$_3$)$_3$ electrodeposition bath; (b) Bubbles inside the foam start to break and are refilled with solvent when the Bi/GF is taken out of the electrodeposition bath; (c) The solvent evaporates from the Bi/GF through capillary transport of liquid and solvent evaporate diffusion; (d) the shrunken Bi foam after drying.

The effects of different post-processing routines were investigated under a) air drying, b) vacuum drying, and c) immersing Bi/GF in water for a few hours followed by air or vacuum drying. The XRD patterns of the Bi/GFs under different post-processing treatments were compared to pristine GF, pure Bi and Bi$_2$O$_3$ powder as illustrated in Figure 7 (a). The wide reflection at about 27° is a typical reflection of GF. The reflections of Bi powder are mainly located at 27.3°, 37.9°, 39.7°, 48.8°, 56.1°, 63°, and 64.6°. More reflections are shown with the Bi$_2$O$_3$ powder within the same 2-theta range. Compared to the patterns of GF and pure Bi powder, the reflections of Bi/GFs under different post-treatments show different degrees of Bi oxidation. The Bi/GFs immersed in water for several hours and then dried under vacuum show a similar pattern to pure Bi powder which indicates that the samples contain mostly metallic Bi. The main reason could be that water immersion helps to flush out the residues from the electrodeposition bath, while vacuum drying lowers the boiling point of the solvent achieving rapid drying as well as helps to eliminate impurities. In contrast, the Bi/GFs under air drying show higher fractions of oxidized Bi. Drying under air is a rather slow process and the impurities from the electrodeposition bath can easily remain inside the pores of the GFs.
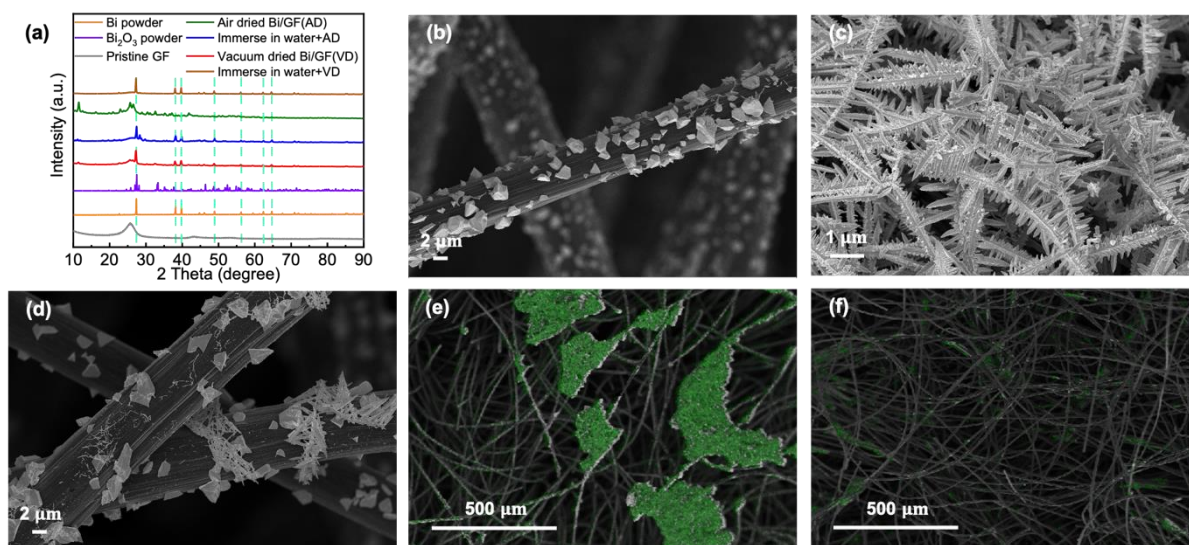
Figure 7. (a) XRD patterns of pristine GF, Bi powder, Bi₂O₃ powder and Bi/GFs under different post-processing and drying conditions. SEM images of DHBT-Bi/GFs (b) graphite fibers under vacuum drying; (c) fern-shaped Bi agglomeration on the surface of GF under vacuum drying; (d) graphite fibers under water immersion followed by vacuum drying. EDX images of Bi distribution on the top surface under (e) vacuum drying; (f) air drying.

Figure 7 (b)-(f) depict the SEM/EDX images of the Bi/GFs under different post-processing and drying conditions. Compared with the uniformly distributed Bi nanoparticles on graphite fibers under air drying shown in Figure 2 (d)-(f) and Figure 7 (f), Bi/GFs under vacuum drying are found to have a non-uniform distribution of Bi and even two different kinds of morphologies. Figure 7 (b) shows large Bi particles on graphite fibers and in Figure 7 (c) striking fern-shaped Bi agglomerations can be observed on the surface of the GF. Figure 7 (e) shows an exemplary EDX mapping of the non-homogeneous Bi distribution on the top surface of Bi/GF under vacuum drying. This morphology should most probably be attributed to the fast drying under vacuum conditions due to the lower boiling point of the solvent. In line with the proposed mechanism presented in Figure 6, solvent vapor diffusion could be the dominant drying process, therefore, not so much Bi has entered the pores of the GF as compared to the Bi/GF under air drying. Since most of the Bi agglomerations appear to be situated near the surface, it can be inferred that only a lower share of Bi nanoparticles is distributed on the fibers inside the GFs. Figure 7 (d) shows an SEM micrograph of the Bi/GFs after water immersion and subsequent vacuum drying. We believe that using water immersion is favorable for washing away the impurities from the electrodeposition bath, but also do observe heterogeneous Bi distribution similar to that of the only vacuum dried samples. During the water immersion process, water could gradually penetrate deeper into the cavities inside the foam and thereby help to build more capillary networks for later drying. Besides, the water may weaken the contact areas and adhesion between the GF and Bi foam. Therefore, for Bi/GFs after immersion in water, the Bi distribution appears non-uniform after drying either under air or vacuum conditions.
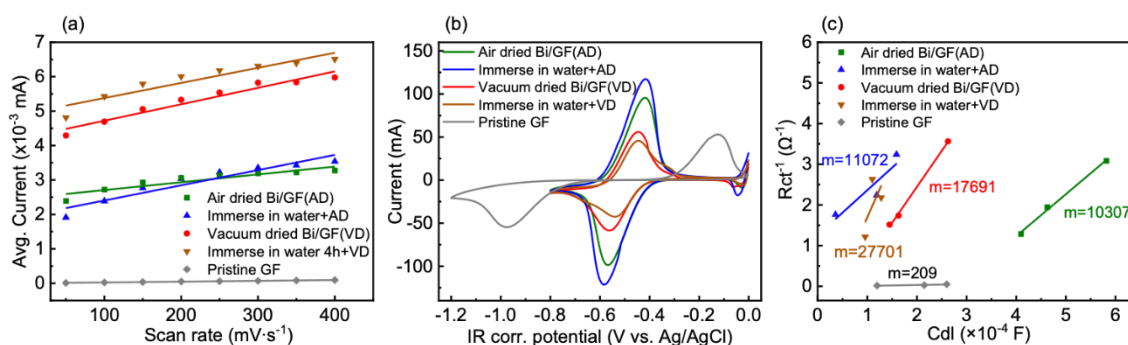
Figure 8. Electrochemical characterization of pristine GF, air-dried Bi/GF, immersion in water followed by air drying Bi/GF, vacuum dried Bi/GF and immersion in water followed by vacuum drying Bi/GF in 3-electrode setup (a) Double layer capacitance current from CV measurements in the non-faradaic region as a function of scan rate. (b) CV curves at the scan rate of 4 mV·s⁻¹. (b) Inverse charge transfer resistance vs. double layer capacitance by normalizing EIS.

To characterize the electrochemical performance of Bi/GFs under different post-processing and drying conditions, DLC vs. scan rate, CV and EIS normalization measurements were performed. Figure 8 (a) shows the double-layer capacitance current as a function of the scan rate of Bi/GFs under different post-processing and drying conditions. The slopes of Bi/GFs are all larger than that of the pristine GF, thus indicating an enhanced ECSA. However, the slope of Bi/GF under air drying is relatively smaller than that of Bi/GFs under the other post-processing treatments. The CV curves of Bi/GFs after different post-treatments are shown in Figure 8 (b). It can be concluded from the curves that the electrochemical activity of the pristine GF for the V^{3+}/V^{2+} redox reaction is poor as indicated by the large peak separation. As for the GFs decorated with DHBT-Bi, they all show very close peak separations which suggest that the reaction kinetics are enhanced due to the electrocatalytic activity of Bi. The Bi/GF immersed in water and then vacuum dried shows the smallest peak separation and with reference to the XRD result, the pattern of this sample is closest to that of the pure Bi powder. It could be inferred that pure Bi catalyses the V^{3+}/V^{2+} redox reactions better than Bi oxides. Besides, the peak currents of Bi/GF under air drying are higher than those under vacuum drying indicating enhanced V^{3+}/V^{2+} conversion. This can be attributed to the better Bi distribution offering more active sites within the GF as a result of the slower drying process under air. Both prolonged water immersion and vacuum drying would keep the Bi foam structure near to the surface. This morphology does not seem to be ideal for electrochemical reactions because the agglomerations near to the top surface can restrict the transport of electroactive species, resulting in difficulties for the electrolyte to reach the inner side of the GFs. This in turn would lead to low utilization of the whole surface area and low redox conversion. Another possible reason is that the Bi agglomerates on the surface act as catalytically active sites with rather fast kinetics, leading to a rapid increase in the thickness of the diffusion layer which then limits the supply of a sufficient amount of redox species. This would also lead to a lower peak current in the CV curve. Figure 8 (c) illustrates the normalized EIS plots of Bi/GFs under different post-processing conditions. The Bi/GF which is immersed in water and then vacuum dried showed the largest slope which indicates the fastest kinetics. This is consistent with the interpretation of the respective CV curves.

3.5 Full-cell measurements

The performance of Bi/GFs under different post-processing conditions was evaluated in a single full-cell setup. The polarization curve and the power density curve are both shown in Figure 9 (a). Compared to the system without Bi (pristine GF), all the systems with Bi show a clear improvement, but to a different extent improvement. Among them, the Bi/GF which has been prepared under air

drying demonstrated the smallest overpotential and the largest power density. This can be attributed to its most uniform Bi distribution onto the graphite fibers of the GF. The redox flow battery utilizing the air-dried Bi/GF is capable of delivering a high power density of 416.6 mW·cm^{-2} at a current density of 480 mA·cm^{-2}. It is assumed that uniform Bi distribution is more important to the full-cell tests. Moreover, there are many other performance-influencing parameters involved in the full-cell setup than the 3-electrode setup, such as possible changes to the Bi foam structure due to 15% compression during the cell assembly, Bi dissolution or washing away under certain flow conditions of the electrolyte, etc. Therefore, the air-dried Bi/GF demonstrated the best performance in contrast to the 3-electrode CV results. Besides, as seen from the polarization curves, the ohmic polarization clearly dominates the voltage losses. Nevertheless, the contact resistance and mass transport in porous electrodes should be reduced in future studies to decrease the voltage losses further.
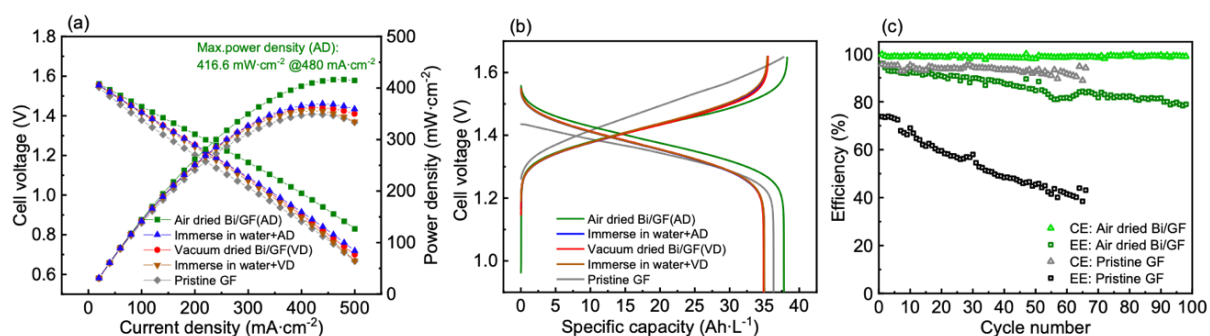

Figure 9. Full-cell measurements of DHBT-Bi/GFs under different post-processing and drying conditions. (a) The polarization and power density curves (b) The charge-discharge curves at a current density of 25 mA·cm^{-2}. (c) The coulombic and energy efficiencies of pristine GF and the air-dried DHBT-Bi/GF.

Figure 9 (b) illustrates the charge and discharge curve of Bi/GFs under different post-processing conditions at a current density of 25 mA·cm^{-2}. The overpotentials for the systems with Bi decrease apparently in the corresponding charge and discharge processes compared to the system without Bi, which suggests the higher electrocatalytic activity of Bi modified GFs. Besides, the Bi/GF under the air drying condition shows a rather high specific capacity which reaches up to 37.5 Ah·L^{-1}. The electrolyte utilization rate is as high as 87.45%. Therefore, a long-term cycling test was conducted with pristine GF and air-dried Bi/GF as the negative electrodes in the full-cell system, as shown in Figure 9 (c). The coulombic efficiency (CE) and energy efficiency (EE) both decrease dramatically in the system with pristine GF due to the large overpotential, whereas Bi/GF maintains a stable CE and EE as the cycle number increases. Regarding the energy efficiency loss per cycle, the system with Bi/GF demonstrates loss rates as low as 0.17%·cycle^{-1}. The full-cell performance seems to be relatively 'moderate' in direct comparison with other publications. One should, however, not overlook the fact that the materials, full-cell setup and testing protocols in this work were chosen and performed under rather realistic conditions, but not at the center of our attention.

4. Conclusions

In this work, Bi-catalyzed negative electrodes for VRFB successfully obtained by the fast and very efficient DHBT synthesis method are presented. The approach involves the galvanostatic deposition of Bi at high current densities accompanied by the evolution of hydrogen bubbles that serve as dynamic templates for the deposition of high surface area Bi on the commercially-applied GFs. CV and EIS normalization results show significant improvements with DHBT synthesis compared to the impregnation of Bi$_2$O$_3$ on GF electrode, and the direct addition of Bi^{3+} into the electrolyte, as reported in previous literature. Different post-processing and drying conditions can lead to different morphologies, ECSA, Bi distributions and impurities, etc. Air drying is a slower

process which helps to better distribute the catalyst onto the fibers and inside the 3-D structured GF than vacuum drying. It was also confirmed that homogenous Bi distribution onto the graphite fibers is a very important parameter for the full-cell performance. Consequently, Bi/GF under air drying showed the highest power density of 416.6 mW·cm^{-2} at a current density of 480 mA·cm^{-2} in the polarization curve. In addition, the electrolyte utilization with an air-dried Bi/GF is as high as 37.5 Ah·L^{-1}. The DHBT-Bi/GF electrode exhibited good stability and energy efficiency of about 78% after 100 cycles at a current density of 25 mA·cm^{-2}.

Author contributions

Ming Cheng: conceptualization, investigation, data curation, methodology, writing—first draft; Tintula Kottakkat: conceptualization, methodology, writing--review and editing; Christina Roth: conceptualization, supervision, writing--review and editing, funding acquisition.

Conflicts of interest
There are no conflicts to declare.

Acknowledgement

References

[1] T. S. Ledley, E. T. Sundquist, S. E. Schwartz, D. K. Hall, J. D. Fellows, and T. L. Killeen, "Climate change and greenhouse gases," *Eos Trans. Am. Geophys. Union*, vol. 80, no. 39, pp. 453–458, Sep. 1999, doi: 10.1029/99EO00325.
[2] N. Kannan and D. Vakeesan, "Solar energy for future world: - A review," *Renew. Sustain. Energy Rev.*, vol. 62, pp. 1092–1105, Sep. 2016, doi: 10.1016/j.rser.2016.05.022.
[3] G. M. Joselin Herbert, S. Iniyan, E. Sreevalsan, and S. Rajapandian, "A review of wind energy technologies," *Renew. Sustain. Energy Rev.*, vol. 11, no. 6, pp. 1117–1145, Aug. 2007, doi: 10.1016/j.rser.2005.08.004.
[4] M. Skyllas-Kazacos, C. Menictas, and T. Lim, "Redox flow batteries for medium- to large-scale energy storage," in *Electricity Transmission, Distribution and Storage Systems*, Elsevier, 2013, pp. 398–441. doi: 10.1533/9780857097378.3.398.
[5] G. Kear, A. A. Shah, and F. C. Walsh, "Development of the all-vanadium redox flow battery for energy storage: a review of technological, financial and policy aspects: All-vanadium redox flow battery for energy storage," *Int. J. Energy Res.*, vol. 36, no. 11, pp. 1105–1120, Sep. 2012, doi: 10.1002/er.1863.
[6] K. Lourenssen, J. Williams, F. Ahmadpour, R. Clemmer, and S. Tasnim, "Vanadium redox flow batteries: A comprehensive review," *J. Energy Storage*, vol. 25, p. 100844, Oct. 2019, doi: 10.1016/j.est.2019.100844.
[7] M. Guarnieri, P. Mattavelli, G. Petrone, and G. Spagnuolo, "Vanadium Redox Flow Batteries: Potentials and Challenges of an Emerging Storage Technology," *IEEE Ind. Electron. Mag.*, vol. 10, no. 4, pp. 20–31, 2016, doi: 10.1109/MIE.2016.2611760.
[8] A. Parasuraman, T. M. Lim, C. Menictas, and M. Skyllas-Kazacos, "Review of material research and development for vanadium redox flow battery applications," *Electrochimica Acta*, vol. 101, pp. 27–40, Jul. 2013, doi: 10.1016/j.electacta.2012.09.067.
[9] C.-N. Sun, F. M. Delnick, D. S. Aaron, A. B. Papandrew, M. M. Mench, and T. A. Zawodzinski, "Probing Electrode Losses in All-Vanadium Redox Flow Batteries with Impedance

Spectroscopy," *ECS Electrochem. Lett.*, vol. 2, no. 5, pp. A43–A45, Feb. 2013, doi: 10.1149/2.001305eel.

[10] T. Greese and G. Reichenauer, "Anode kinetics degradation in vanadium redox flow batteries – Reversible inhibition of the V2+/V3+-reaction due to V(II)-adsorption," *J. Power Sources*, vol. 500, p. 229958, Jul. 2021, doi: 10.1016/j.jpowsour.2021.229958.

[11] C.-N. Sun, F. M. Delnick, D. S. Aaron, A. B. Papandrew, M. M. Mench, and T. A. Zawodzinski, "Resolving Losses at the Negative Electrode in All-Vanadium Redox Flow Batteries Using Electrochemical Impedance Spectroscopy," *J. Electrochem. Soc.*, vol. 161, no. 6, pp. A981–A988, 2014, doi: 10.1149/2.045406jes.

[12] B. Srnv, "MODIFICATION OF GRAPHITE ELECTRODE MATERIALS FOR VANADIUM REDOX FLOW BATTERY APPLICATION-I. THERMAL TREATMfiNT," p. 8.

[13] B. Sun and M. Skyllas-Kazacos, "Chemical modification of graphite electrode materials for vanadium redox flow battery application—part II. Acid treatments," *Electrochimica Acta*, vol. 37, no. 13, pp. 2459–2465, Oct. 1992, doi: 10.1016/0013-4686(92)87084-D.

[14] X. L. Zhou, Y. K. Zeng, X. B. Zhu, L. Wei, and T. S. Zhao, "A high-performance dual-scale porous electrode for vanadium redox flow batteries," *J. Power Sources*, vol. 325, pp. 329–336, Sep. 2016, doi: 10.1016/j.jpowsour.2016.06.048.

[15] B. Li *et al.*, "Bismuth Nanoparticle Decorating Graphite Felt as a High-Performance Electrode for an All-Vanadium Redox Flow Battery," *Nano Lett.*, vol. 13, no. 3, pp. 1330–1335, Mar. 2013, doi: 10.1021/nl400223v.

[16] H. R. Jiang, Y. K. Zeng, M. C. Wu, W. Shyy, and T. S. Zhao, "A uniformly distributed bismuth nanoparticle-modified carbon cloth electrode for vanadium redox flow batteries," *Appl. Energy*, vol. 240, pp. 226–235, Apr. 2019, doi: 10.1016/j.apenergy.2019.02.051.

[17] J. Schneider *et al.*, "Degradation Phenomena of Bismuth-Modified Felt Electrodes in VRFB Studied by Electrochemical Impedance Spectroscopy," *Batteries*, vol. 5, no. 1, p. 16, Jan. 2019, doi: 10.3390/batteries5010016.

[18] Z. Yang, Y. Wei, Y. Zeng, and Y. Yuan, "Effects of in-situ bismuth catalyst electrodeposition on performance of vanadium redox flow batteries," *J. Power Sources*, vol. 506, p. 230238, Sep. 2021, doi: 10.1016/j.jpowsour.2021.230238.

[19] H. R. Jiang, J. Sun, L. Wei, M. C. Wu, W. Shyy, and T. S. Zhao, "A high power density and long cycle life vanadium redox flow battery," *Energy Storage Mater.*, vol. 24, pp. 529–540, Jan. 2020, doi: 10.1016/j.ensm.2019.07.005.

[20] S. Moon, B. W. Kwon, Y. Chung, and Y. Kwon, "Effect of Bismuth Sulfate Coated on Acidified CNT on Performance of Vanadium Redox Flow Battery," *J. Electrochem. Soc.*, vol. 166, no. 12, pp. A2602–A2609, 2019, doi: 10.1149/2.1181912jes.

[21] X. Zhou, X. Zhang, L. Mo, X. Zhou, and Q. Wu, "Densely Populated Bismuth Nanosphere Semi-Embedded Carbon Felt for Ultrahigh-Rate and Stable Vanadium Redox Flow Batteries," *Small*, vol. 16, no. 37, p. 1907333, Sep. 2020, doi: 10.1002/smll.201907333.

[22] A. Fetyan, G. A. El-Nagar, I. Derr, P. Kubella, H. Dau, and C. Roth, "A neodymium oxide nanoparticle-doped carbon felt as promising electrode for vanadium redox flow batteries," *Electrochimica Acta*, vol. 268, pp. 59–65, Apr. 2018, doi: 10.1016/j.electacta.2018.02.104.

[23] W. H. Wang and X. D. Wang, "Investigation of Ir-modified carbon felt as the positive electrode of an all-vanadium redox flow battery," *Electrochimica Acta*, vol. 52, no. 24, pp. 6755–6762, Aug. 2007, doi: 10.1016/j.electacta.2007.04.121.

[24] L. Wei, T. S. Zhao, L. Zeng, Y. K. Zeng, and H. R. Jiang, "Highly catalytic and stabilized titanium nitride nanowire array-decorated graphite felt electrodes for all vanadium redox flow batteries," *J. Power Sources*, vol. 341, pp. 318–326, Feb. 2017, doi: 10.1016/j.jpowsour.2016.12.016.

[25] D. Cheng, G. Cheng, Z. He, L. Dai, and L. Wang, "Electrocatalytic performance of TiO$_2$ with different phase state towards V^{2+}/V^{3+} reaction for vanadium redox flow battery," *Int. J. Energy Res.*, vol. 43, no. 9, pp. 4473–4482, Jul. 2019, doi: 10.1002/er.4575.

[26] P. C. Ghimire *et al.*, "Titanium carbide-decorated graphite felt as high performance negative electrode in vanadium redox flow batteries," *J. Mater. Chem. A*, vol. 6, no. 15, pp. 6625–6632, 2018, doi: 10.1039/C8TA00464A.

[27] J. Kumberg *et al.*, "Drying of Lithium-Ion Battery Anodes for Use in High-Energy Cells: Influence of Electrode Thickness on Drying Time, Adhesion, and Crack Formation," *Energy Technol.*, vol. 7, no. 11, p. 1900722, Nov. 2019, doi: 10.1002/ente.201900722.

[28] H.-C. Shin and M. Liu, "Copper Foam Structures with Highly Porous Nanostructured Walls," *Chem. Mater.*, vol. 16, no. 25, pp. 5460–5464, Dec. 2004, doi: 10.1021/cm048887b.

[29] A. Dutta, C. E. Morstein, M. Rahaman, A. Cedeño López, and P. Broekmann, "Beyond Copper in CO_2 Electrolysis: Effective Hydrocarbon Production on Silver-Nanofoam Catalysts," *ACS Catal.*, vol. 8, no. 9, pp. 8357–8368, Sep. 2018, doi: 10.1021/acscatal.8b01738.

[30] A. Dutta *et al.*, "A Tandem ($Bi_2O_3 \rightarrow Bi_{met}$) Catalyst for Highly Efficient *ec*-CO_2 Conversion into Formate: *Operando* Raman Spectroscopic Evidence for a Reaction Pathway Change," *ACS Catal.*, vol. 11, no. 9, pp. 4988–5003, May 2021, doi: 10.1021/acscatal.0c05317.

[31] Y. Li, Y.-Y. Song, C. Yang, and X.-H. Xia, "Hydrogen bubble dynamic template synthesis of porous gold for nonenzymatic electrochemical detection of glucose," *Electrochem. Commun.*, vol. 9, no. 5, pp. 981–988, May 2007, doi: 10.1016/j.elecom.2006.11.035.

[32] M.-G. Jeong, K. Zhuo, S. Cherevko, W.-J. Kim, and C.-H. Chung, "Facile preparation of three-dimensional porous hydrous ruthenium oxide electrode for supercapacitors," *J. Power Sources*, vol. 244, pp. 806–811, Dec. 2013, doi: 10.1016/j.jpowsour.2012.12.037.

[33] J. Friedl and U. Stimming, "Determining Electron Transfer Kinetics at Porous Electrodes," *Electrochimica Acta*, vol. 227, pp. 235–245, Feb. 2017, doi: 10.1016/j.electacta.2017.01.010.

[34] H. Fink, J. Friedl, and U. Stimming, "Composition of the Electrode Determines Which Half-Cell's Rate Constant is Higher in a Vanadium Flow Battery," *J. Phys. Chem. C*, vol. 120, no. 29, pp. 15893–15901, Jul. 2016, doi: 10.1021/acs.jpcc.5b12098.

[35] B. J. Plowman, L. A. Jones, and S. K. Bhargava, "Building with bubbles: the formation of high surface area honeycomb-like films via hydrogen bubble templated electrodeposition," *Chem. Commun.*, vol. 51, no. 21, pp. 4331–4346, 2015, doi: 10.1039/C4CC06638C.